King Saud University

**Journal of Saudi Chemical Society**

## ORIGINAL ARTICLE

# Facile synthesis of porous $Fe_2O_3$ nanorods and their photocatalytic properties

CrossMark

Xiaosi Liu [a,1], Kaikai Chen [b,1], Jae-Jin Shim [b,*], Jiarui Huang [a,b,*]

[a] College of Chemistry and Materials Science, Center for Nano Science and Technology, Anhui Normal University, Wuhu, Anhui 241000, People's Republic of China
[b] School of Chemical Engineering, Yeungnam University, Gyeongsan, Gyeoungbuk 712749, Republic of Korea

**Abstract** Porous $Fe_2O_3$ nanorods were obtained using a facile chemical solution method with subsequent calcination. The structures and morphological evolution were characterized by X-ray diffraction, field emission scanning electron microscopy, thermogravimetric-differential thermal analysis, and Brunauer–Emmett–Teller (BET) $N_2$ adsorption–desorption analyses. The calculated BET surface area of the porous $Fe_2O_3$ nanorods was 18.8 $m^2 g^{-1}$. The porous $Fe_2O_3$ nanorods were used as a catalyst to photodegrade Rhodamine B, methylene blue, methyl orange, p-nitrophenol, and eosin B. Compared to the commercial $Fe_2O_3$ powder, the as-prepared porous $Fe_2O_3$ nanorods exhibited higher catalytic activities owing to their large surface areas and porous nanostructures. The photocatalytic reaction rate constant of the porous $Fe_2O_3$ nanorods in the photocatalytic decomposition of Rhodamine B under simulated solar light was calculated to be 0.0131 $min^{-1}$. Moreover, the catalyst was found to have superior stability and reusability.

© 2015 King Saud University. Production and hosting by Elsevier B.V. This is an open access article under the CC BY-NC-ND license (http://creativecommons.org/licenses/by-nc-nd/4.0/).

## 1. Introduction

Textile dyes with high aromaticity and low biodegradability are major environmental pollutants [1,2]. A large quantity of organic dyes are used in printing, textile, paper and pharmaceutical industries. During these dying processes, a significant fraction of these dyes are lost and released into water streams. In many situations, dye molecules are non-biodegradable, so it is important to mineralize them in aqueous solutions. The photocatalytic degradation of organic pollutants based on inorganic semiconductors has attracted considerable attention because they show promise for solving environmental pollution problems [3–5]. Recently, nanostructured materials have attracted considerable interest owing to their unique properties and potential applications [6–9]. Therefore, the

* Corresponding authors at: College of Chemistry and Materials Science, Center for Nano Science and Technology, Anhui Normal University, Wuhu, Anhui 241000, People's Republic of China (J.R. Huang). Tel.: +82 53 810 2587; fax: +82 53 810 4631.
E-mail addresses: jjshim@yu.ac.kr (J.-J. Shim), jrhuang@mail.ahnu.edu.cn (J. Huang).
[1] Equal contribution as the first author.
Peer review under responsibility of King Saud University.
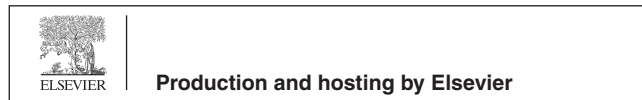
decomposition of organic pollutants using various nanomaterials in the presence of sunlight has been a major topic. $TiO_2$, a wide band gap semiconductor, is one of the most effective photocatalysts for the degradation of organic and inorganic pollutants as well as other toxic materials under ultraviolet (UV) light irradiation [10]. Nanocomposites can improve the visible light photocatalytic activities of wide band gap semiconductors. For example, Cho et al. developed $TiO_2$ nanoparticles, $Au@TiO_2$ and $Ag@TiO_2$ nanocomposites for the catalytic degradation of dyes under visible light irradiation [11–13]. Furthermore, Cho et al. also reported $Au@CeO_2$ and $Ag@CeO_2$ nanocomposites that possessed excellent visible light photocatalytic activities [14,15]. Several kinds of ZnO based nanocomposites also possessed excellent visible light photocatalytic activities [16–20]. Although several types of visible light-active photocatalysts have been obtained, it is important to explore new types of photocatalysts under visible light irradiation.

Iron oxide ($\alpha$-$Fe_2O_3$, hematite) is a promising material for photocatalytic applications owing to its narrow band gap of approximately 2.2 eV, chemical stability and nontoxicity, which absorbs light up to 600 nm, collects up to 40% of the solar spectrum energy, and might be one of the cheapest semiconductor materials [21]. By absorbing visible light, the electrons of $\alpha$-$Fe_2O_3$ are excited from the valence band to the conduction band. These excited electrons and the corresponding holes can activate the surrounding chemical species and promote the chemical reactions [22]. For practical applications, photocatalysts with a high surface area and favorable recyclability are expected. Recently, nanostructuring techniques have proven to be useful for increasing the performance of $\alpha$-$Fe_2O_3$ for the photo-response, and a unique surface shape, such as quantum dots and nanorods, can be expected to increase the photoactive surface; hence, enhance the photocatalytic activity [23–27]. In fact, the particle size of $\sim$10 nm was close to the regime, where the quantum size effect is prominent. The band positions will move and higher redox potentials of the free electrons and holes will be achieved in this regime, which in turn enhance the charge-transfer rates in the materials. The increase in the charge transfer rates reduces the direct recombination rate of the charge carriers drastically, which may explain why smaller size particles show higher photocatalytic performance. Therefore, low-dimensional nanoscale materials may improve the photocatalytic properties for the degradation of organic pollutants owing to their special structure, morphology, size and spatial arrangement, and quantum confinement.

## 2. Photocatalysis measurement

The photocatalytic activities of the porous $Fe_2O_3$ nanorods (the synthesis procedure is given in Fig. S1 in Supporting materials) and commercial $Fe_2O_3$ powder (SEM image is given in Fig. S1 in Supporting materials) were evaluated according to the removal of the model dye pollutants such as RhB, methylene blue (MB), p-nitrophenol (pNP), eosin B, and methyl orange (MO) from the solution. The photocatalytic experiments were carried out by adding 15 mg of the porous $Fe_2O_3$ nanorods or commercial $Fe_2O_3$ powder into 50 mL of the organic dye aqueous solution with a concentration of 10 mg/L. The suspension was ultrasonicated for 30 min, and then stirred for another 30 min in the dark to obtain the adsorption equilibrium of the dye molecules before

illumination. The suspension was then irradiated with a 500 W Xe lamp (Shanghai Jiguang Special Light, China) with a dominant wavelength from 250 nm to 1000 nm to simulate solar irradiation. During the full irradiation process, the suspension was stirred continuously. At a given time interval, 3 mL of the suspension was removed and centrifuged immediately to eliminate the solid particles. The changes in the optical properties of the dyes were recorded on a Hitachi U-3010 UV–vis absorption spectrophotometer (Tokyo, Japan) at the maximum absorbance peak. The maximum absorption wavelengths of RhB, MB, pNP, eosin B, and MO were 552 nm, 665 nm, 320 nm, 517 nm, and 462 nm, respectively. Using the same method, the photodegradation rates of the other pollutants in the presence of porous $Fe_2O_3$ nanorods and commercial $Fe_2O_3$ powder were also measured.

## 3. Results and discussion

### 3.1. Structure and morphology

The porous $Fe_2O_3$ nanorods were produced using a two-step procedure. First, the ferrous oxalate dihydrate (FOD, $FeC_2O_4 \cdot 2H_2O$) nanorod precursor was obtained from a chemical solution process. Subsequent calcination of the precursor yielded the porous $Fe_2O_3$ nanorods. The crystal phase of the FOD precursor was characterized by XRD, and the data are shown in Fig. S2a. All the diffraction peaks of the precursor were assigned to monoclinic $FeC_2O_4 \cdot 2H_2O$ (JCPDS 72-1305). The reactions in the synthesis of FOD nanorod precursor could be formulated simply as follows:

$$FeSO_4 + H_2C_2O_4 + 2NaOH = FeC_2O_4 \cdot 2H_2O$$
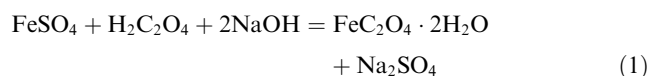$$+ Na_2SO_4 \qquad (1)$$

Fig. S2b shows that the XRD pattern of the sample heat-treated to 500 °C in air for 2 h is completely different from that of the precursor. The characteristic peaks of the rhombohedral phase $Fe_2O_3$ (JCPDS 89-2810) were observed. This suggests that the $FeC_2O_4 \cdot 2H_2O$ decomposed and rhombohedral phase $Fe_2O_3$ was formed when the sample was heated in air to 500 °C.

The morphology of the precursor before and after calcination was characterized by FESEM. Fig. S3 shows FESEM images of the FOD precursor and the corresponding $Fe_2O_3$ product after calcination. At lower magnification (Fig. S3a), the precursor consisted of a large quantity of uniform rod-like nanostructures with typical lengths ranging from 3 μm to 9 μm. The diameter of the FOD nanorods was in the range, 110–150 nm (Fig. S3b). After the thermal decomposition process, the rod-like morphology remained intact, as shown in Figs. S3c and S3d. On the other hand, nanometer-sized porous architectures were observed as shown in the high magnification image (Fig. S3d). The irregular pores of tens of nanometers were distributed randomly in the nanorods due to thermal decomposition of the FOD precursor.

Fig. S4a presents a typical transmission electron microscopy (TEM) image of the porous $Fe_2O_3$ nanorods. The diameter of the porous $Fe_2O_3$ nanorods was ca. 120 nm. Furthermore, the TEM images (Fig. S4b) confirmed the high porosity of the $Fe_2O_3$ nanorods, which resulted from thermal decomposition of the FOD precursor. Fig. S4c shows the HRTEM image of the porous $Fe_2O_3$ nanorods. The distance

between the parallel lattices was measured to be 0.368 nm, corresponding to the (1 1 0) crystal planes of the rhombohedral phase Fe$_2$O$_3$. A SAED pattern with some irregular dots, as shown in Fig. S4d, also suggests a polycrystalline nature.

To validate the inner architectures of porous Fe$_2$O$_3$ nanorods, nitrogen adsorption and desorption measurements were performed to estimate the textural properties. Fig. S5 presents the nitrogen adsorption and desorption isotherm and pore size distribution curve (inset) of the porous Fe$_2$O$_3$ nanorods calcined at 500 °C. The isotherm of the porous Fe$_2$O$_3$ nanorod sample exhibited a hysteresis loop at $p/p_0$ range, 0.87–0.97, which is associated with the filling up and emptying of the mesopores by capillary condensation. This clearly suggests that the porous Fe$_2$O$_3$ nanorod sample exhibits large textural porosity. The pore size distribution of the porous Fe$_2$O$_3$ nanorods shows a broad peak in the pore size region from 5.0 nm to 50.1 nm. Using the Barett–Joyner–Halenda method and the desorption branch of the nitrogen isotherm, the calculated pore size distribution indicated that the material had a mean pore size of 14.2 nm. Pores of various sizes were previously observed in FESEM and TEM images, in accordance with these stochastic calculation results. The BET surface area of the porous Fe$_2$O$_3$ nanorods assessed by the BET method was 18.8 m$^2$ g$^{-1}$, which is higher than that of commercial Fe$_2$O$_3$ powder (7.7 m$^2$ g$^{-1}$). As a result of the large surface area and mesoporous structure, the as-prepared porous Fe$_2$O$_3$ nanorods have provided numerous active sites for surface contact reactions, highlighting their potential applications to photocatalysis with excellent performance.

The optical properties of the as-synthesized porous Fe$_2$O$_3$ nanorods and commercial Fe$_2$O$_3$ powder were examined by UV–vis spectroscopy. As shown in Fig. S6, the porous Fe$_2$O$_3$ nanorods and commercial Fe$_2$O$_3$ powder showed band edge absorptions at approximately 610 nm and 620 nm, respectively. Fe$_2$O$_3$ is a n-type semi-conductor and the absorption band gap ($E_g$) can be determined from the following equation: $(\alpha h v)^2 = K(h v - E_g)$, where $h v$ is the photon energy (eV), $A$ is the absorption coefficient, $a$ is a constant and $E_g$ is the band gap. $E_g$ was found to be 2.15 eV, from the intercept of the straight line plot of $(\alpha h v)^2$ vs. $h v$ at $\alpha = 0$, which is blue shifted relative to the characteristic band gap energy of the commercial Fe$_2$O$_3$ powder ($E_g = 2.05$ eV). The higher band gap compared to the commercial Fe$_2$O$_3$ powder was attributed to the decreasing particle size.

### 3.2. Photocatalytic properties of the porous Fe$_2$O$_3$ nanorods

To evaluate the photocatalytic activity of the product, the optical property changes of a RhB aqueous solution in the presence of porous Fe$_2$O$_3$ nanorods and commercial Fe$_2$O$_3$ powder under simulated solar irradiation for a constant time were measured. Fig. 1 presents the time-dependent absorption spectra of the RhB solution containing the porous Fe$_2$O$_3$ nanorod catalyst during the irradiation. Without a catalyst, only a slow decrease in the concentration of RhB was detected under the simulated solar irradiation (see Fig. 1b). On the other hand, when porous Fe$_2$O$_3$ nanorods and commercial Fe$_2$O$_3$ powder were added to the reaction system, the degradation of RhB could be accelerated obviously. Fig. 1a shows that the maximum absorbance at 552 nm decreases rapidly with irradiation time. The absorption intensity of the peak
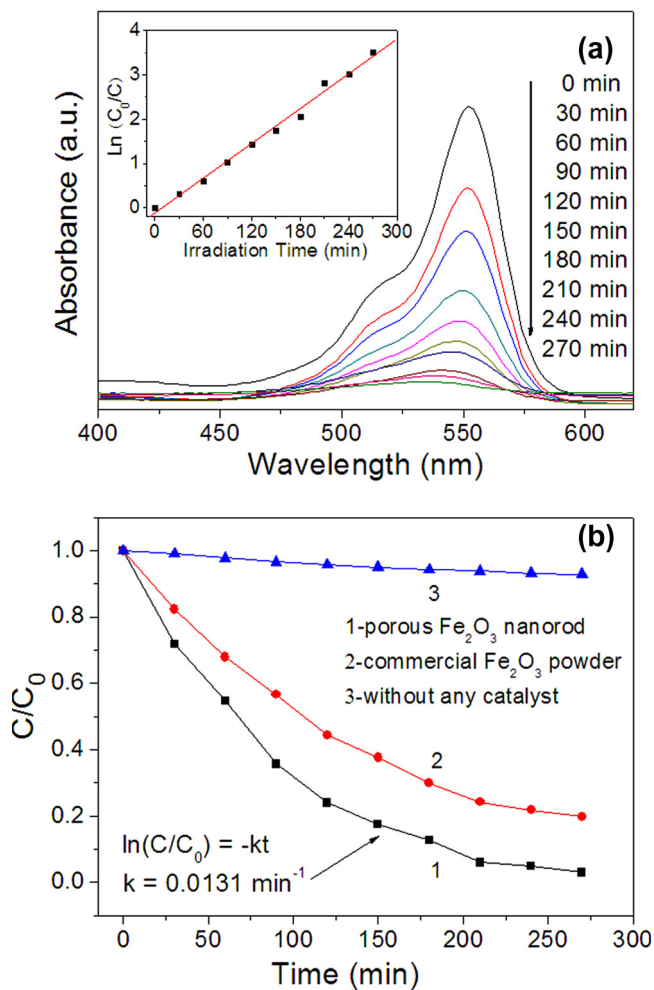


**Figure 1** (a) Changes in the absorbance spectra of the RhB in aqueous solution (10 mg/L, 50 mL) in the presence of porous Fe$_2$O$_3$ nanorods under the simulated solar light; (b) Photodegradation plots of RhB under the simulated solar light for different times in the presence/absence of the catalysts.

was reduced by approximately 28.1% when the solution had been irradiated under simulated solar light for 30 min in the presence of porous Fe$_2$O$_3$ nanorods. After 90 min, the degree of bleaching was 64.3%. After 180 min, the degree of bleaching reached up to 87.2%, and after 270 min, the degree of bleaching reached 97.0%. The absorption peak disappeared almost completely, indicating that most of the RhB had been degraded. The bleaching of the solution can be due to the destruction of the dye chromogen. As no new absorption peak was observed, the RhB is believed to have been decomposed completely. By monitoring the RhB absorption peak at 552 nm, plots of the degradation ratio vs. reaction time were obtained in the absence of a catalyst under identical conditions. The degradation ratio was calculated with $(1 - C_t/C_0)$. The normalized concentration of the solution equals the normalized maximum absorbance, so $C_0/C$ was used to take place of $A_0/A$, where $C_0$ and $C$ are the initial and actual concentration of RhB, respectively. The photocatalytic decomposition of RhB solution agrees with the pseudo-first-order kinetics [28]. As a result, the rate constants ($k$) can be calculated using the
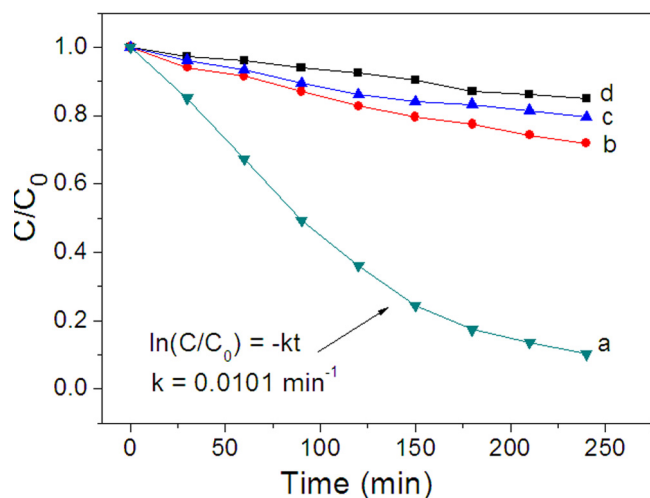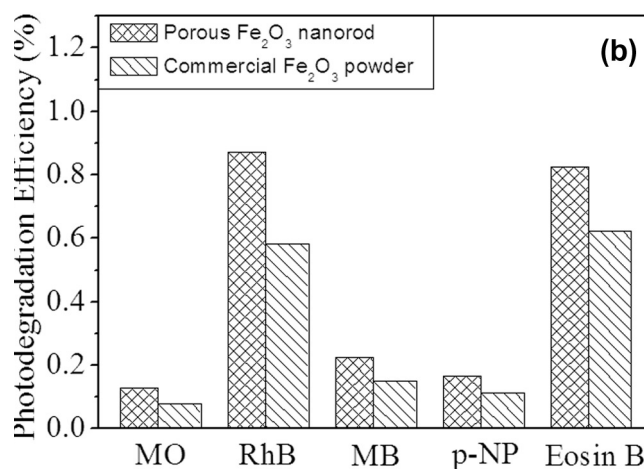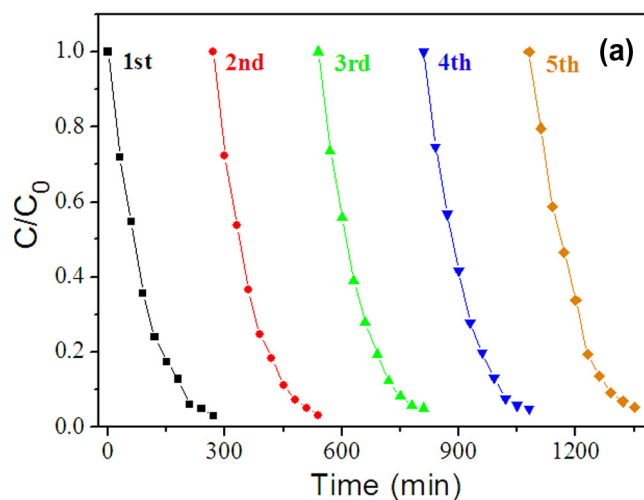
**Figure 2** Photodegradation plots of (a) eosin B, (b) MB, (c) p-nitrophenol, and (d) MO under the simulated solar light in the presence of the porous $Fe_2O_3$ nanorod catalyst, in which $C$ is the concentration of RhB and $C_0$ is the initial concentration.

equation: $\ln(C/C_0) = -kt$. The photocatalytic reaction rate constant of RhB in the presence of porous $Fe_2O_3$ nanorods under simulated solar light was calculated to be 0.0131 $min^{-1}$. The catalytic activity of the porous $Fe_2O_3$ nanorods was higher than that of the commercial $Fe_2O_3$ powder.

The photocatalytic properties for the degradation of RhB suggest that the as-prepared porous $Fe_2O_3$ nanorods have potential applications in water treatment. The catalytic process is mainly related to the adsorption and desorption of molecules on the catalyst surface. After irradiating the porous $Fe_2O_3$ nanorods with visible light, the valance-band (VB) electrons ($e^-$) of the $Fe_2O_3$ are ejected into the conduction-band (CB), generating holes ($h^+$) in the valence band. The photo-generated holes can react with adsorbed water on the surface of the porous $Fe_2O_3$ nanorods to generate the highly reactive hydroxyl radical (OH·), while $O_2$ acts as an electron acceptor to form a superoxide anion radical ($O_2^-$). Further the $O_2^-$ can act as an oxidizing agent or as an additional source of OH·. These reactive radicals have strong oxidizing ability and are able to degrade the RhB dye into non-toxic organic compounds [29]. Without the porous $Fe_2O_3$ nanorods, some RhB dye molecules were stimulated to excited state under visible light irradiation. The excited RhB molecules will release electrons when they react with the oxygen molecules dissolved in solution, while $O_2$ acts as an electron acceptor to form a superoxide anion radical ($O_2^-$). Further the $O_2^-$ can act as an oxidizing agent or as an additional source of OH·. Therefore, the porous $Fe_2O_3$ nanorods promote the photodegradation process of RhB dye under visible light irradiation. Compared to the commercial $Fe_2O_3$ powder, the high specific surface area (18.8 $m^2 g^{-1}$) of the porous $Fe_2O_3$ nanorods results in a larger number of unsaturated surface coordination sites exposed to the solution. Therefore, the porous $Fe_2O_3$ nanorods with large surface areas and small crystal size can provide more active reaction sites and facilitates the separation of electron-hole pairs during the photochemical reaction.

In addition to the degradation of RhB, the porous $Fe_2O_3$ nanorods were also used in photocatalytic degradation of



**Figure 3** (a) Catalyst recycling in the degradation of RhB in the presence of porous $Fe_2O_3$ nanorod catalyst, in which $C$ is the concentration of RhB and $C_0$ is the initial concentration. (b) Photodegradation efficiencies of five kinds of dye pollutants under simulated solar irradiation in 180 min in the presence of the porous $Fe_2O_3$ nanorods and commercial $Fe_2O_3$ powder, respectively.

other dye pollutants under simulated solar irradiation, as shown in Fig. 2. It can be seen that eosin B was also effectively decomposed under the same experimental conditions as those used in the degradation of RhB. After 30 min, the decoloring degree of aqueous eosin B reached 14.9%, and after 60 min, the decoloring degree achieved 32.7%. After 90 min, the decoloring degree was up to 50.7%, and after 210 min, the decoloring degree achieved 86.4%. The fitting of absorbance maximum plot versus time indicates an exponential decay. The photocatalytic reaction rate constant of eosin B in the presence of the porous $Fe_2O_3$ nanorods under simulated solar light was calculated to be 0.0101 $min^{-1}$. However, the porous $Fe_2O_3$ nanorods exhibited low photocatalytic activities to MB, p-nitrophenol, and MO under the simulated solar light. The order of degradation rate for all used dyes was as follows: RhB > eosin B > MB > pNP > MO. The porous $Fe_2O_3$ nanorods exhibited high photocatalytic degradation performance for RhB and eosin B, which is mainly due to the high absorbability of the porous $Fe_2O_3$ nanorods for RhB and eosin

B. In addition, the porous Fe$_2$O$_3$ nanorods can exhibit various photocatalytic degradation performances for the dye pollutants under different pH values, because the pH value of the dye solution can affect the absorbability of the porous Fe$_2$O$_3$ nanorods for the dye pollutants. This will be investigated in our further studies.

The stability and reusability of the catalysts are very important issues for practical applications. The porous Fe$_2$O$_3$ nanorods could be recycled readily by simple centrifugation after the reaction. The stability and reusability of the porous Fe$_2$O$_3$ nanorods were examined by the repetitive use of the catalyst. As shown in Fig. 3a, the catalysts did not exhibit a significant loss of activity after five photodegradation cycles of RhB. The photocatalysts after the reusability experiments were further analyzed by XRD and SEM to study the photostability of the porous Fe$_2$O$_3$ nanorods. It was found that the crystalline structure remained unaltered after the photodegradation experiments, indicating their high photostability. The SEM results of the used samples were also found to be the same morphologies as those of the fresh samples after the photodegradation.

For comparison, commercial Fe$_2$O$_3$ powder was also used in photocatalytic degradation of the dye pollutants under simulated solar irradiation, as shown in Fig. 3b. Approximately 7.9% MO, 15.2% MB, 11.3% pNP, and 62.4% eosin B were decomposed in the presence of the commercial Fe$_2$O$_3$ powder in 180 min. The photodegradation ratios of MO, RhB, MB, pNP, and eosin B in the presence of the porous Fe$_2$O$_3$ nanorods under simulated solar irradiation in 180 min were 12.8%, 22.5%, 16.7%, and 82.6%, respectively, which are much higher than those in the presence of commercial Fe$_2$O$_3$ powder. Obviously, the porous Fe$_2$O$_3$ nanorods showed different activities in the photodegradation of these dye pollutants, but their presence enhanced the degradation of all pollutants mentioned above because of their large surface areas and porous nanostructures.

## 4. Conclusions

Porous Fe$_2$O$_3$ nanorods were synthesized using a surfactant-free chemical solution method combined with a subsequent annealing process. The as-prepared porous Fe$_2$O$_3$ nanorods exhibited high photocatalytic activities in the photodegradation of RhB and eosin B. The photocatalytic reaction rate constant of RhB under the simulated solar light was 0.0131 min$^{-1}$. Compared to the commercial Fe$_2$O$_3$ powder, the as-prepared porous Fe$_2$O$_3$ nanorods exhibited higher catalytic activities. The excellent photocatalytic property of the porous Fe$_2$O$_3$ nanorods benefited substantially from their unique porous nanostructures, which provides more active reaction sites and facilitates the separation of electron-hole pairs during the photochemical reaction.

## Acknowledgements

## Appendix A. Supplementary data

## References

[1] T. Sauer, G.C. Neto, H.J. Jose, R.F.P.M. Moreira, Kinetics of photocatalytic degradation of reactive dyes in a TiO$_2$ slurry reactor, J. Photochem. Photobiol. A 149 (2002) 147–154.

[2] A.K. Dutta, S.K. Maji, B. Adhikary, Γ-Fe$_2$O$_3$ nanoparticles: an easily recoverable effective photo-catalyst for the degradation of rose Bengal and methylene blue dyes in the waste-water treatment plant, Mater. Res. Bull. 49 (2014) 28–34.

[3] J.R. Huang, H.B. Ren, X.S. Liu, X.X. Li, J.-J. Shim, Facile synthesis of porous TiO$_2$ nanospheres and their photocatalytic properties, Superlattices Microstruct. 81 (2015) 16–25.

[4] L. Karimi, S. Zohoori, M.E. Yazdanshenas, Photocatalytic degradation of azo dyes in aqueous solutions under UV irradiation using nano-strontium titanate as the nanophotocatalyst, J. Saudi Chem. Soc. 18 (2014) 581–588.

[5] M.A. Habib, I.M.I. Ismail, A. Mahmood, M.R. Ullah, Photocatalytic decolorization of Brilliant Golden Yellow in TiO$_2$ and ZnO suspensions, J. Saudi Chem. Soc. 16 (2012) 423–429.

[6] J.R. Huang, H.B. Ren, K.K. Chen, J.J. Shim, Controlled synthesis of porous Co$_3$O$_4$ micro/nanostructures and their photocatalysis property, Superlattices Microstruct. 75 (2014) 843–856.

[7] J.R. Huang, G.J. Fu, C.C. Shi, X.Y. Wang, M.H. Zhai, C.P. Gu, Novel porous CuO microrods: synthesis, characterization, and their photocatalysis property, J. Phys. Chem. Solids 75 (2014) 1011–1016.

[8] J.R. Huang, H.B. Ren, P.P. Sun, C.P. Gu, Y.F. Sun, J.H. Liu, Facile synthesis of porous ZnO nanowires consisting of ordered nanocrystallites and their enhanced gas-sensing property, Sens. Actuator B 188 (2013) 249–256.

[9] J.R. Huang, Y.Y. Wang, C.P. Gu, M.H. Zhai, Large scale synthesis of uniform CuS nanotubes by a sacrificial templating method and their application as an efficient photocatalyst, Mater. Lett. 99 (2013) 31–34.

[10] S.H. Xu, W.F. Shangguan, J. Yuan, J.W. Shi, M.X. Chen, Photocatalytic properties of bismuth titanate Bi$_{12}$TiO$_{20}$ prepared by co-precipitation processing, Mater. Sci. Eng. B 137 (2007) 108–111.

[11] M.M. Khan, S.A. Ansari, D. Pradhan, M.O. Ansari, D.H. Han, J. Lee, M.H. Cho, Band gap engineered TiO$_2$ nanoparticles for visible light induced photoelectrochemical and photocatalytic studies, J. Mater. Chem. A 2 (2014) 637–644.

[12] M.M. Khan, J. Lee, M.H. Cho, Au@TiO$_2$ nanocomposites for the catalytic degradation of methyl orange and methylene blue: an electron relay effect, J. Ind. Eng. Chem. 20 (2014) 1584–1590.

[13] M.M. Khan, S.A. Ansari, M.I. Amal, J. Lee, M.H. Cho, Highly visible light active Ag@TiO$_2$ nanocomposites synthesized using an electrochemically active biofilm: a novel biogenic approach, Nanoscale 5 (2013) 4427–4435.

[14] M.M. Khan, S.A. Ansari, M.O. Ansari, B.K. Min, J. Lee, M.H. Cho, Biogenic fabrication of Au@CeO$_2$ nanocomposite with enhanced visible light activity, J. Mater. Chem. C 118 (2014) 9477–9484.

[15] M.M. Khan, S.A. Ansari, J.H. Lee, M.O. Ansari, J. Lee, M.H. Cho, Electrochemically active biofilm assisted synthesis of Ag@CeO$_2$ nanocomposites for antimicrobial activity, photocatalysis and photoelectrodes, J. Colloid Interface Sci. 431 (2014) 255–263.

[16] R. Saravanan, V.K. Gupta, V. Narayanan, A. Stephen, Visible light degradation of textile effluent using novel catalyst ZnO/γ-Mn$_2$O$_3$, J. Taiwan Inst. Chem. E 45 (2014) 1910–1917.

[17] R. Saravanan, M.M. Khan, V.K. Gupta, E. Mosquera, F. Gracia, V. Narayanan, A. Stephen, ZnO/Ag/Mn$_2$O$_3$ nanocomposite for visible light induced industrial textile effluent degradation, uric acid and ascorbic acid sensing and antimicrobial activity, RSC Adv. 5 (2015) 34645–34651.

[18] R. Saravanan, M.M. Khan, V.K. Gupta, E. Mosquera, F. Gracia, V. Narayanan, A. Stephen, ZnO/Ag/CdO nanocomposite for visible light-induced photocatalytic degradation of industrial textile effluents, J. Colloid Interface Sci. 452 (2015) 126–133.

[19] R. Saravanan, H. Shankar, T. Prakash, V. Narayanan, A. Stephen, ZnO/CdO composite nanorods for photocatalytic degradation of methylene blue under visible light, Mater. Chem. Phys. 125 (2011) 277–280.

[20] R. Saravanan, S. Karthikeyan, V.K. Gupta, G. Sekaran, V. Narayanan, A. Stephen, Enhanced photocatalytic activity of ZnO/CuO nanocomposite for the degradation of textile dye on visible light illumination, Mater. Sci. Eng. C 33 (2013) 91–98.

[21] G.K. Mor, H.E. Prakasam, O.K. Varghese, K. Shankar, C.A. Grimes, Vertically oriented Ti−Fe−O nanotube array films toward a useful material architecture for solar spectrum water photoelectrolysis, Nano Lett. 7 (2007) 2356–2364.

[22] D.S. Bohle, C.J. Spina, Cationic and anionic surface binding sites on nanocrystalline zinc oxide: surface influence on photoluminescence and photocatalysis, J. Am. Chem. Soc. 131 (2009) 4397–4404.

[23] Y. Liang, C.S. Enache, R.V.D. Krol, Photoelectrochemical characterization of sprayed alpha Fe$_2$O$_3$ thin films: influence of Si doping and interfacial layer, Int. J. Photoenergy 73 (2008) 739864.

[24] F. Ahmed, N. Arshi, M.S. Anwar, R. Danish, B.H. Koo, Quantum-confinement induced enhancement in photocatalytic properties of iron oxide nanoparticles prepared by Ionic liquid, Ceram. Int. 40 (2014) 15743–15751.

[25] X.L. Cui, T. Liu, Z.Q. Zhang, L. Wang, S.Q. Zuo, W.C. Zhu, Hematite nanorods with tunable porous structure: facile hydrothermal-calcination route synthesis, optical and photocatalytic properties, Powder Technol. 266 (2014) 113–119.

[26] R. Suresh, K. Giribabu, R. Manigandan, A. Vijayaraj, R. Prabu, A. Stephen, V. Narayanan, Alpha-Fe$_2$O$_3$ nanoflowers: synthesis, characterization, electrochemical sensing and photocatalytic property, Iran Chem. Soc. 11 (2014) 645–652.

[27] J.R. Huang, M. Yang, C.P. Gu, M.H. Zhai, Y.F. Sun, J.H. Liu, Hematite solid and hollow spindles: selective synthesis and application in gas sensor and photocatalysis, Mater. Res. Bull. 46 (2011) 1211–1218.

[28] M.R. Bayati, F. Golestani-Fard, A.Z. Moshfegh, Visible photodecomposition of methylene blue over micro arc oxidized WO$_3$–loaded TiO$_2$ nano-porous layers, Appl. Catal. A 382 (2010) 322–331.

[29] C.C. Chen, W. Zhao, P.X. Lei, J.C. Zhao, N. Serpone, Photosensitized degradation of dyes in polyoxometalate solutions versus TiO$_2$ dispersions under visible-light irradiation: mechanistic implications, Chem. Eur. J. 10 (2004) 1956–1965.